Light transport in biological tissue using three-dimensional frequency-domain simplified spherical harmonics equations

2009 Phys. Med. Biol. 54 2493

(http://iopscience.iop.org/0031-9155/54/8/016)

IOP PUBLISHING PHYSICS IN MEDICINE AND BIOLOGY

Phys. Med. Biol. **54** (2009) 2493–2509 doi:10.1088/0031-9155/54/8/016

Light transport in biological tissue using three-dimensional frequency-domain simplified spherical harmonics equations

Michael Chu[1], **Karthik Vishwanath**[2], **Alexander D Klose**[3] **and Hamid Dehghani**[4]

[1] School of Physics, University of Exeter, Exeter EX4 1EZ, UK
[2] Department of Biomedical Engineering, Duke University, NC 27708, USA
[3] Department of Radiology, Columbia University, NY 10032, USA
[4] School of Computer Science, University of Birmingham, Birmingham B15 2TT, UK

E-mail: mc283@ex.ac.uk

Received 1 December 2008, in final form 27 February 2009
Published 1 April 2009
Online at stacks.iop.org/PMB/54/2493

Abstract

The accuracy of the commonly used diffusion approximation as used in diffuse optical tomography is known to be limited in cases involving strong absorption and in these situations a higher ordered approximation is necessary. In this study, a light transport model has been developed based upon the three-dimensional frequency-domain simplified spherical harmonics (SP_N) approximation for orders up to $N = 7$. The SP_N data are tested against a semi-infinite multi-layered Monte Carlo model. It has been shown that the SP_N approximation for higher orders ($N > 1$) provides an increase in accuracy over the diffusion equation specifically near sources and at boundaries of regions with increased optical absorption. It is demonstrated that the error of fluence calculated near the sources between the diffusion approximation and the SP_N model ($N = 7$) can be as large as 60%, therefore limiting the use of the diffusion approximation for small animal imaging and in situations where optical changes near sources are critical for tomographic reconstructions.

(Some figures in this article are in colour only in the electronic version)

1. Introduction

Near-infrared (NIR) optical tomography is a non-invasive imaging modality in which the optical properties within a volume of interest can be reconstructed using measured transmission and reflectance NIR data. These calculated optical maps can then be used to derive functional and structural information about the tissue being imaged (Gibson *et al* 2005). Due to the relatively low absorption of haemoglobin, water and lipid at a wavelength range of

650 nm–1000 nm, NIR light can transmit through several centimetres of tissue with an adequate signal-to-noise ratio to allow tomographic detection of light transmission. Using the measured NIR signal, together with the known spectral absorption and scatter coefficients of tissue, it is possible to extract functional information about the tissue being imaged (Corlu *et al* 2005, Srinivasan *et al* 2005, Dehghani *et al* 2008).

Several imaging modalities have arisen with specific application for biological tissue, including breast cancer detection and characterization (Ntziachristos *et al* 2000, Jiang *et al* 2001, Dehghani *et al* 2003b, Choe *et al* 2005, Enfield *et al* 2007) and brain functional imaging (Bluestone *et al* 2001, Hebden *et al* 2004, Zeff *et al* 2007). More recently the use of biological markers for function specific optical imaging has led to the development of novel imaging systems and algorithms that aim to recover images of function specific activity within small animals using, for example fluorescence (Mang *et al* 1993, Sevick-Muraca *et al* 1997, Klose and Hielscher 2003, Ntziachristos 2006) or bioluminescence markers (Contag and Bachmann 2002, Alexandrakis *et al* 2005, Dehghani *et al* 2006, Wang *et al* 2006, Kuo *et al* 2007, Klose and Beattie 2008).

Most NIR imaging studies have relied on the use of model-based image reconstruction algorithms whereby the propagation of the NIR signal within the imaging domain is approximated to provide a match (through the use of appropriate optimization) with measured boundary data (Arridge 1999, Hielscher *et al* 1999). A large number of different models can be used to predict light propagation within tissue, including stochastic, analytical and numerical. Stochastic models involve predicting individual photon interactions using either explicit or implicit methods. Two of the most common methods include the Monte Carlo (MC) methods (Wang *et al* 1995) and random walk theory (Gandjbakhche and Weiss 1995). Analytical models have the advantage of being computationally fast but suffer from the disadvantage of being limited to simple geometries with nearly homogeneous interior values. Numerical models have the potential of being able to model complex geometries as well as complex heterogeneous media, but historically required longer computation times. But perhaps the most promising reason for adoption of numerical approaches is to facilitate the combination of NIR tomography with standard clinical imaging systems, using pre-defined tissue geometries as the input domain. A number of different numerical models have been developed and used with specific application in diffuse optical tomography (DOT), including finite elements (Arridge *et al* 1993, Jiang and Paulsen 1995, Schweiger *et al* 1995, Gao *et al* 1998, Jiang 1998, Dehghani *et al* 2003a), finite difference (Hielscher *et al* 1998, Klose and Hielscher 1999), finite volume (Ren *et al* 2004) and boundary elements (Zacharopoulos *et al* 2006, Srinivasan *et al* 2007).

It is generally accepted that if the magnitude of the isotropic fluence within tissue is significantly larger than the directional flux magnitude, the light field is in effect ‘diffuse’, which occurs when the scattering interactions dominate over absorption and the region of interest is far from sources and boundaries, provided that the light fluence is not rapidly changing with time (i.e. such as in the sub-picosecond time frame). This assumption allows a transition from the radiative transport equation (RTE), which is used to describe an anisotropic light field to the diffusion approximation, which is used for isotropic fluence fields (Arridge 1999).

A major drawback of the use of the RTE is the complex implementation within a numerical setting and the large number of resulting equations that need to be solved. One specific challenge is the use of an appropriate method for the incorporation of the angular dependence of the problem. The discrete-ordinates (S_N) method (Chandrasekhar 1950) is widely used with several different finite difference approximations (Lathrop 1972) such as the diamond difference scheme, the weighted diamond difference scheme, the centred difference scheme

(Reed 1971) or the step-difference scheme (Case and Zweifel 1967). However, discrete-ordinates methods require exactly $N(N+2)$ equations to be solved where N is the number of direction cosines.

Another common approach is the use of spherical harmonics (P_N) expansion, whereby the angular dependence can be described by a set of spherical harmonics (Case and Zweifel 1967). Advanced modelling and image reconstruction techniques using the P_N approximation have been demonstrated for the orders of $N = 1$, 3, 5 and 7 (Wright *et al* 2007). This study showed through simulated data that the quality of reconstructed images for a small domain can be improved for higher order N. In 3D problems, however, the P_N approximation requires a set of $(N+1)^2$ coupled equations, where N is the number of Legendre polynomials. More recently, the simplified spherical harmonics (SP_N) method has been applied (Klose and Larsen 2006) which requires just $(N+1)/2$ equations.

The use of SP_N methods has been demonstrated to give accurate solutions for small geometries and in cases where the source/detector separation is small. Specifically, the method has been shown to significantly improve the solution in domains with high absorption and small geometries and is less computationally expensive (Klose and Larsen 2006).

This paper presents the advancement of using simplified spherical harmonics (SP_N) which has been previously reported for continuous-wave (CW) systems (Klose and Larsen 2006). Specifically, we present the development, implementation and validation of a three-dimensional (3D) frequency-domain (FD) model, based on the SP_N equations. It is demonstrated that although the solution using the SP_N method is asymptotic, the use of higher order approximations provides a much more accurate solution, specifically near source locations, which may be of importance when dealing with imaging of small volumes and specifically in situations whereby changes near the sources are required to be determined in, for example, bioluminescence imaging.

Through direct comparisons with Monte Carlo models, it is demonstrated that in such cases as discussed above, SP_N models where $N > 1$ provide much more accurate results as compared to the diffusion equation, i.e. $N = 1$.

2. Theory

2.1. Radiative transport equation

By treating light as photons, and thus ignoring any wave effects, the propagation of light in tissue can be well described by the radiative transport equation:

$$\hat{\mathbf{s}} \cdot \nabla I(\mathbf{r}, \omega, \hat{\mathbf{s}}) + \left(\mu_a + \mu_s + \frac{\mathrm{i}\omega}{c}\right) I(\mathbf{r}, \omega, \hat{\mathbf{s}}) = \mu_s \int_{4\pi} f(\hat{s} \cdot \hat{s}') I(\mathbf{r}, \omega, \hat{\mathbf{s}}')\, \mathrm{d}^2\hat{\mathbf{s}}' + q(\mathbf{r}, \omega, \hat{\mathbf{s}}), \tag{1}$$

where $I(\mathbf{r}, \omega, \hat{\mathbf{s}})$ is the radiance at point $\mathbf{r}$ at modulation frequency ω and in the direction $\hat{\mathbf{s}}$. μ_a and μ_s are the absorption and scattering coefficients respectively, and c is the speed of light in the medium. The $f(\hat{\mathbf{s}} \cdot \hat{\mathbf{s}}')$ term is the scattering phase function, which characterizes the intensity of a beam which is scattered from the direction $\hat{\mathbf{s}}'$ into the direction $\hat{\mathbf{s}}$. The scattering phase function most typically employed is the commonly used Henyey–Greenstein scattering function (Welch and Van Gemert 1995, Klose *et al* 2002, Tarvainen *et al* 2005):

$$f(\cos\theta) = \frac{1}{4\pi}\left[\frac{1 - g^2}{(1 + g^2 - 2g\cos\theta)^{3/2}}\right], \tag{2}$$

where θ is the angle between the two directions $\hat{\mathbf{s}}$ and $\hat{\mathbf{s}}'$, and g is the anisotropy factor which is used to characterize the angular distribution of tissue scattering. The fluence at point $\mathbf{r}$,

modulation frequency ω and in the direction $\hat{\mathbf{s}}$ is defined by

$$\phi(r,\omega) = \int_{4\pi} I(r,\omega,\hat{s})\,\mathrm{d}\hat{s}. \tag{3}$$

2.2. *Simplified spherical harmonics approximation*

The simplified spherical harmonics approximation has the potential to provide an increase in accuracy over standard diffusion models in cases involving highly absorbing regions, which was originally applied to nuclear reactor problems (Gelbard 1968). The initial derivation involved taking the planar version of the spherical harmonics approximation to the RTE and replacing the 1D derivatives with their 3D counterparts. Due to the weak theory of this derivation, the SP_N approximations were not widely accepted until the 1990s when similar equations were found using an asymptotic analysis (Larsen *et al* 1996) and has only recently been applied to optical imaging problems (Klose and Larsen 2006).

In this work, the SP_N approximations have been implemented for 3D frequency-domain measurements. The extension from the continuous-wave SP_N equations (Klose and Larsen 2006) to frequency-domain equations involves the use of the complex-valued absorption moments as defined in equation (5).

The coupled equations for $N = 7$ have been found to be

$$-\nabla.\frac{1}{3\mu_{a1}}\nabla\varphi_1 + \mu_a\varphi_1 = Q + \frac{2}{3}\mu_a\varphi_2 - \frac{8}{15}\mu_a\varphi_3 + \frac{16}{35}\mu_a\varphi_4 \tag{4a}$$

$$-\nabla.\frac{1}{7\mu_{a3}}\nabla\varphi_2 + \left(\frac{4}{9}\mu_a + \frac{5}{9}\mu_{a2}\right)\varphi_2 = -\frac{2}{3}Q + \frac{2}{3}\mu_a\varphi_1 + \left(\frac{16}{45}\mu_a + \frac{4}{9}\mu_{a2}\right)\varphi_3 - \left(\frac{32}{105}\mu_a + \frac{8}{21}\mu_{a2}\right)\varphi_4 \tag{4b}$$

$$-\nabla.\frac{1}{11\mu_{a5}}\nabla\varphi_3 + \left(\frac{64}{225}\mu_a + \frac{16}{45}\mu_{a2} + \frac{9}{25}\mu_{a4}\right)\varphi_3 = \frac{8}{15}Q - \frac{8}{15}\mu_a\varphi_1 + \left(\frac{16}{45}\mu_a + \frac{4}{9}\mu_{a2}\right)\varphi_2 + \left(\frac{128}{525}\mu_a + \frac{32}{105}\mu_{a2} + \frac{54}{175}\mu_{a4}\right)\varphi_4 \tag{4c}$$

$$-\nabla.\frac{1}{15\mu_{a7}}\nabla\varphi_4 + \left(\frac{256}{1225}\mu_a + \frac{64}{245}\mu_{a2} + \frac{324}{1225}\mu_{a4} + \frac{13}{49}\mu_{a6}\right)\varphi_4 = -\frac{16}{35}Q + \frac{16}{35}\mu_a\varphi_1 - \left(\frac{32}{105}\mu_a + \frac{8}{21}\mu_{a2}\right)\varphi_2 + \left(\frac{128}{525}\mu_a + \frac{32}{105}\mu_{a2} + \frac{54}{175}\mu_{a4}\right)\varphi_3 \tag{4d}$$

where Q is the isotropic source term, φ_n is the composite moment of the fluence and μ_{an} is the nth-order complex absorption coefficient given by

$$\mu_{an}(x) = \mu_t(x) + \frac{\mathrm{i}\omega}{c} - \mu_s(x)g^n, \tag{5}$$

where the total attenuation coefficient μ_t is given by the sum of the absorption and scattering coefficients ($\mu_a + \mu_s$). The complex nature of the attenuation coefficient arises from the fact that radiance will also vary due to the modulation frequency, with the effect of making the absorption coefficient complex.

For convenience, the composite moments of the fluence are defined as

$$\varphi_1 = \phi_0 + 2\phi_2 \tag{6a}$$

$$\varphi_2 = 3\phi_2 + 4\phi_4 \tag{6b}$$

$$\varphi_3 = 5\phi_4 + 6\phi_6 \tag{6c}$$

$$\varphi_4 = 7\phi_6 \tag{6d}$$

and the total fluence Φ is then given by

$$\phi = \varphi_1 - \tfrac{2}{3}\varphi_2 + \tfrac{8}{15}\varphi_3 - \tfrac{16}{35}\varphi_4. \tag{7}$$

The SP_1 approximation can then be found by setting $\phi_6 = \phi_4 = \phi_2 = 0$ and solving equation (4*a*). The SP_3 approximation can be found by solving equations (4*a*) and (4*b*) with $\phi_6 = \phi_4 = 0$ and the SP_5 approximation can be found by setting $\phi_6 = 0$ and solving equations (4*a*)–(4*c*). It can therefore be seen that the SP_1 case simplifies to the diffusion equation.

2.3. Boundary conditions

Depending on the angle of incidence, photons attempting to cross the boundary, at $r \in \partial\Omega$ (where Ω is the domain of interest), will either pass through at a refracted angle defined by Snell's law or will be reflected back into the domain. The probability of a photon being reflected is given by

$$R(\cos\theta') = \begin{cases} \dfrac{1}{2}\left(\dfrac{n_m\cos\theta'' - n_0\cos\theta'}{n_m\cos\theta'' + n_0\cos\theta'}\right)^2 + \dfrac{1}{2}\left(\dfrac{n_m\cos\theta' - n_0\cos\theta''}{n_m\cos\theta' + n_0\cos\theta''}\right)^2 & \theta' < \theta_c \\ 1 & \theta' \geqslant \theta_c, \end{cases} \tag{8}$$

where θ' is the internal angle, θ'' is the refracted angle and θ_c is the critical angle, n_m is the refractive index within the tissue and n_0 is the refractive index of air ($n_0 = 1$). The boundary conditions are therefore found to be

$$\left(\frac{1}{2} + A_1\right)\varphi_1 + \left(\frac{1 + B_1}{3\mu_{a1}}\right)\mathbf{n}\cdot\varphi_1 = \left(\frac{1}{8} + C_1\right)\varphi_2 + \left(\frac{D_1}{\mu_{a3}}\right)\mathbf{n}\cdot\varphi_2 + \left(-\frac{1}{16} + E_1\right)\varphi_3 + \left(\frac{F_1}{\mu_{a5}}\right)\mathbf{n}\cdot\varphi_3 + \left(\frac{5}{128} + G_1\right)\varphi_4 + \left(\frac{H_1}{\mu_{a7}}\right)\mathbf{n}\cdot\varphi_4 + \int_{\Omega\cdot n<0} S(\Omega)2|\Omega\cdot\mathbf{n}|\,\mathrm{d}\Omega \tag{9a}$$

$$\left(\frac{7}{24} + A_2\right)\varphi_2 + \left(\frac{1 + B_2}{7\mu_{a3}}\right)\mathbf{n}\cdot\varphi_2 = \left(\frac{1}{8} + C_2\right)\varphi_1 + \left(\frac{D_2}{\mu_{a1}}\right)\mathbf{n}\cdot\varphi_1 + \left(\frac{41}{384} + E_2\right)\varphi_3 + \left(\frac{F_2}{\mu_{a5}}\right)\mathbf{n}\cdot\varphi_3 + \left(-\frac{1}{16} + G_2\right)\varphi_4 + \left(\frac{H_2}{\mu_{a7}}\right)\mathbf{n}\cdot\varphi_4 + \int_{\Omega\cdot n<0} S(\Omega)(5|\Omega\cdot\mathbf{n}|^3 - 3|\Omega\cdot\mathbf{n}|)\,\mathrm{d}\Omega \tag{9b}$$

$$\left(\frac{407}{1920} + A_3\right)\varphi_3 + \left(\frac{1 + B_3}{11\mu_{a4}}\right)\mathbf{n}\cdot\varphi_3 = \left(-\frac{1}{16} + C_3\right)\varphi_1 + \left(\frac{D_3}{\mu_{a1}}\right)\mathbf{n}\cdot\varphi_1 + \left(\frac{41}{384} + E_3\right)\varphi_2 + \left(\frac{F_3}{\mu_{a3}}\right)\mathbf{n}\cdot\varphi_2 + \left(\frac{233}{2560} + G_3\right)\varphi_4 + \left(\frac{H_3}{\mu_{a7}}\right)\mathbf{n}\cdot\varphi_4 + \int_{\Omega\cdot n<0} S(\Omega)\left(\frac{63}{4}|\Omega\cdot\mathbf{n}|^5 - \frac{35}{2}|\Omega\cdot\mathbf{n}|^3 + \frac{15}{4}|\Omega\cdot\mathbf{n}|\right)\mathrm{d}\Omega \tag{9c}$$

$$\left(\frac{3023}{17\,920}+A_4\right)\varphi_4+\left(\frac{1+B_4}{15\mu_{a7}}\right)\mathbf{n}\cdot\varphi_4=\left(\frac{5}{128}+C_4\right)\varphi_1+\left(\frac{D_4}{\mu_{a1}}\right)\mathbf{n}\cdot\varphi_1+\left(-\frac{1}{16}+E_4\right)\varphi_2$$
$$+\left(\frac{F_4}{\mu_{a3}}\right)\mathbf{n}\cdot\varphi_2+\left(\frac{233}{2560}+G_4\right)\varphi_3+\left(\frac{H_4}{\mu_{a5}}\right)\mathbf{n}\cdot\varphi_3$$
$$+\int_{\Omega\cdot n<0}S(\Omega)\left(\frac{429}{8}|\Omega\cdot\mathbf{n}|^7-\frac{693}{8}|\Omega\cdot\mathbf{n}|^5+\frac{315}{8}|\Omega\cdot\mathbf{n}|^3-\frac{35}{8|\Omega\cdot\mathbf{n}|}\right)\mathrm{d}\Omega. \tag{9d}$$

The coefficients A_n–H_n used in these equations are related to various orders of reflectivity and can be calculated for different values of refractive index. Again, the only extension from continuous-wave to frequency-domain boundary conditions is the use of the complex-valued absorption moments (Klose and Larsen 2006).

2.4. Finite element implementation

The finite element discretization of a domain Ω can be obtained by subdividing the domain into D elements joined at V vertex nodes. In finite element formalism, $\Phi(\mathbf{r})$ is approximated by the piecewise continuous polynomial function $\Phi^h(r,w)=\sum_i^V\Phi_i u_i(r)\Omega^h$, where Ω^h is a finite-dimensional subspace spanned by basis functions $\{u_i(r);\, i=1,\ldots,V\}$ chosen to have limited support. The problem of solving for Φ^h becomes one of sparse matrix inversion: in this work, we use bi-conjugate gradients stabilized solver. Equations (4*a*)–(4*d*) can then be represented using matrices:

$$(K_1+C+F_1)\varphi_1=Q+(C_1+G_1)\varphi_2-(C_2+H_1)\varphi_3+(C_3+I_1)\varphi_4 \tag{10a}$$

$$(K_3+C_4+C_5+F_2)\varphi_2=-\tfrac{2}{3}Q+(C_1+G_2)\varphi_1+(C_6+C_7+H_2)\varphi_3-(C_8+C_9+I_2)\varphi_4 \tag{10b}$$

$$(K_5+C_{10}+C_{11}+C_{12}+F_3)\varphi_3=\tfrac{8}{15}Q-(C_2+G_3)\varphi_1+(C_6+C_7+H_3)\varphi_2$$
$$+(C_{13}+C_{14}+C_{15}+I_3)\varphi_4 \tag{10c}$$

$$(K_7+C_{16}+C_{17}+C_{18}+C_{19}+F_4)\varphi_4=-\tfrac{16}{35}Q+(C_3+G_4)\varphi_1-(C_8+C_9+H_4)\varphi_2$$
$$+(C_{13}+C_{14}+C_{15}+I_4)\varphi_3 \tag{10d}$$

where the C matrices represent the various orders and fractions of μ_{an}, the F, G, H and I matrices represent the boundary terms and the K matrices represent the diffusion terms with the form $\frac{1}{\alpha\mu_{an}}$, where $\alpha=3$, 7, 11 or 15.

Equations (10*a*)–(10*d*) can then be rearranged into a single matrix equation of the form

$$\begin{bmatrix}M_{11}&\cdots&\cdots&M_{14}\\ \vdots&\ddots&\ddots&\vdots\\ \vdots&\ddots&\ddots&\vdots\\ M_{41}&\cdots&\cdots&M_{44}\end{bmatrix}\begin{bmatrix}\varphi_1\\ \varphi_2\\ \varphi_3\\ \varphi_4\end{bmatrix}=\begin{bmatrix}Q_1\\ -\frac{2}{3}Q_2\\ \frac{8}{15}Q_3\\ -\frac{16}{35}Q_4\end{bmatrix} \tag{11}$$

where the M_{ij} terms are as defined in the appendix, and represent combinations of system matrices in equations (10*a*)–(10*d*). This allows the solution for φ_1, φ_2, φ_3 and φ_4 to be found simultaneously using just one matrix inversion.

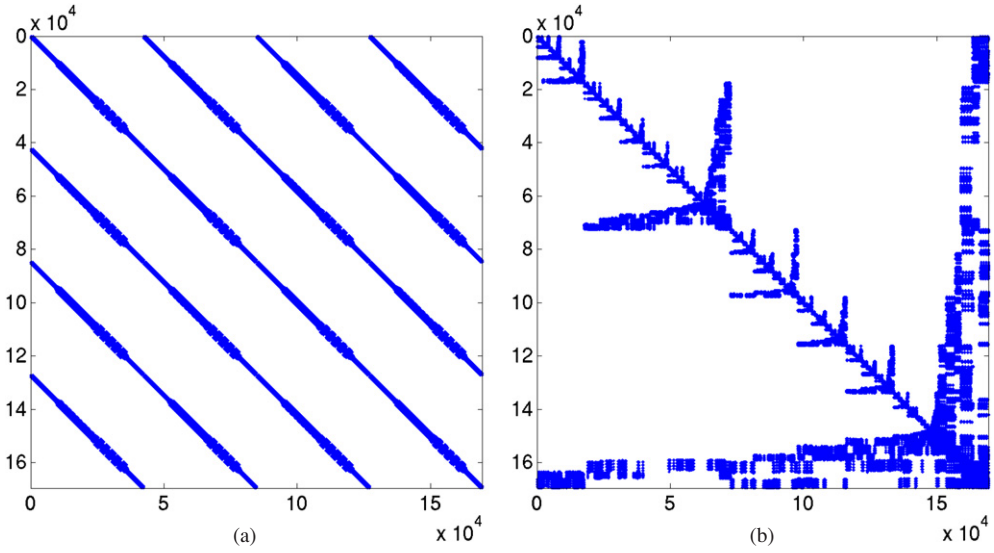

Figure 1. Pattern of non-zeros in the MASS matrix equation (13) (a) before and (b) after reordering. The x- and y-axes correspond to the length of the square matrix in equation 11, which is 169 544 (total number of nodes in mesh $\times$ 4).

2.5. Optimization through matrix reordering

The cost associated with solving sparse matrix problems depends not only on their sparsity but also on the distribution of the non-zero elements within that matrix. To minimize the fill-in phenomenon due to the decomposition of the Mass matrix into equation (11) (left-hand side), the matrix is reordered (optimized) using symmetric approximate minimum degree permutation (AMD) that produces a matrix with a sparser Cholesky factor as compared to the original matrix. Typical distributions of the non-zero elements in the Mass matrix before and after reordering are shown in figure 1, using MATLAB's implementation of functions for sparse matrix operations (symamd) (Amestoy *et al* 2004).

2.6. Monte Carlo modelling

A Monte Carlo model to simulate propagation of light in a semi-infinite turbid medium was extended to photon propagation in a stratified medium as described previously (Wang *et al* 1995, Vishwanath *et al* 2002). Briefly, the turbid medium was modelled as having layers of finite thickness (along the z-axis) with specified transport coefficients and refractive indices in each layer. Photons were incident normally at the top face of the turbid medium. For every scattering event where the calculated step size (along a particular direction) caused a photon to cross a boundary, the photon was first propagated to the point where its trajectory intersected the boundary via a shortened step-size. The angle of incidence with respect to the $\pm z$-axis (depending on the direction of photon travel) was computed and used to determine if the photon suffered total internal reflection (from Snell's law). If the photon was internally reflected, then the z-component of the photon's travel direction was reversed and the photon completed the remainder of the step in the same layer, otherwise the reflection coefficient from Fresnel's equations was computed and compared against a uniformly generated random number. For every sampling of the random number that was less than the reflection coefficient,

Table 1. The computation times of the SP_N models using an FEM mesh consisting of 42 386 nodes forming 235 869 tetrahedral elements. The models were run on a 3.0 GHz, 64 bit Linux system with 8 GB of physical memory using Matlab R2007b. The SP_5 and SP_7 models required the use of swap space and as such the computation time was considerably slower than expected.

	Computation time (min)
SP_1	4.2
SP_3	12.6
SP_5	31.7
SP_7	69.7
Monte Carlo	28

the photon underwent total internal reflection; otherwise it was transmitted to the next layer (or escaped from the domain). On transmission into a different layer the final spatial location of the photon was calculated by propagating the photon by a distance that was adjusted in length (to account for the difference in transport coefficients between the two layers) and its direction corrected to consider refraction. All photons emanating from the top layer of the turbid medium were spatially and temporally binned to calculate the reflectance from a turbid medium. Photons were collected at set radial distances from the source, assuming a numerical aperture of 1, and were then normalized with respect to the collecting area to give a point-like measurement. The temporal data were recorded at a resolution of 10 ns. The resulting temporal data were then Fourier transformed to give frequency-domain estimates of the amplitude and phase shift as a function of distance, in order to match the type of data used in our work.

3. Methods and results

In the following sections, we compare results from the developed SP_N model ($N = 1$, 3, 5 and 7) and the MC model for a simple 3D slab of either homogenous or layered optical properties. For the MC results, the number of simulated photons was 1×10^6, with a total execution time of approximately 20–40 min (table 1). All calculations were performed on a dual core 3.0 GHz, 64 bit Linux system with 8 GB physical memory.

The validity of the diffusion approximation, and hence the SP_1 model in large medium problems and in cases where scattering dominates absorption, has been previously shown demonstrating its validity by use of phantom data (Dehghani *et al* 2003a) as well as Monte Carlo data (Dehghani *et al* 2003a). The work presented here, therefore, concentrated on small volume domains and in cases of strong absorption, whereby the diffusion approximation is less valid.

The model domain used was a 3D slab of width and length of 40 mm (x-coordinates) with a thickness of 20 mm (y-coordinates) and a depth of 30 mm (z-coordinates) (figure 2). The source was placed at the centre of the top most surface boundary and boundary reflectance measurements were made at 1 mm distances from 3 to 10 mm away from the source. The source was modelled as a point source on the surface of the external boundary to most appropriately match the MC model, which used a collimated source located on the surface. The FEM mesh used in this study contained 42 386 nodes corresponding to 235 869 linear tetrahedral elements. The resolution of the mesh was increased in the areas surrounding the source in order to increase the numerical accuracy of the solution whilst minimizing the computational resources required. Table 1 shows the computational time and memory requirements to solve the various SP_N models as well as the MC.

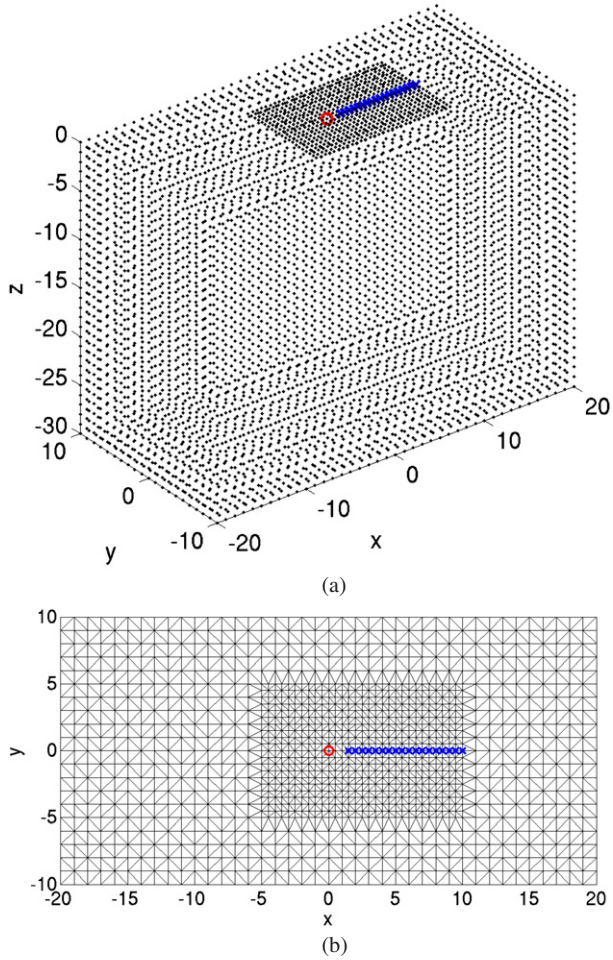

Figure 2. 3D mesh used for the calculation of data using the SPN models: (a) 3D view of the surface nodes and (b) 2D representation of the top surface. The circle represents the location of the source and the cross represents the location of the detectors.

Three individual cases were considered using both MC and SP_N models. In the first case, a homogenous medium with optical properties of $\mu_a = 0.001\ \text{mm}^{-1}$, $\mu_s = 2.0\ \text{mm}^{-1}$, $g = 0.5$ and $n_m = 1.37$ and the solutions to SP_1, SP_3, SP_5 and SP_7 were calculated using the methods outlined in section 2, with the computation times as shown in table 1. The calculated amplitude and phase of the reflectance boundary data, from the 3D model (figure 2) and the semi-infinite MC model, are shown in figure 3. It can be seen that for both the amplitude and phase of the boundary data, the SP_7 approximation provides the closest match with the MC data, whereas the SP1 approximation (the diffusion approximation) provides the worst match. The error between the SP_N method and MC data is also seen to reduce, specifically for the phase, at measurement points furthest away from the source as the number of spherical moments is increased. The calculated amplitude data for SP_1 near the source appear to underestimate the solution as compared to the MC, whereas the higher approximations have overestimated the amplitude. The calculated 3D fluence from SP_7 and SP_1 was also used to calculate the percentage error map (error $= 100 \times (\Phi_{SP1} - \Phi_{SP7})/\Phi_{SP7}$), with the 2D cross-section at

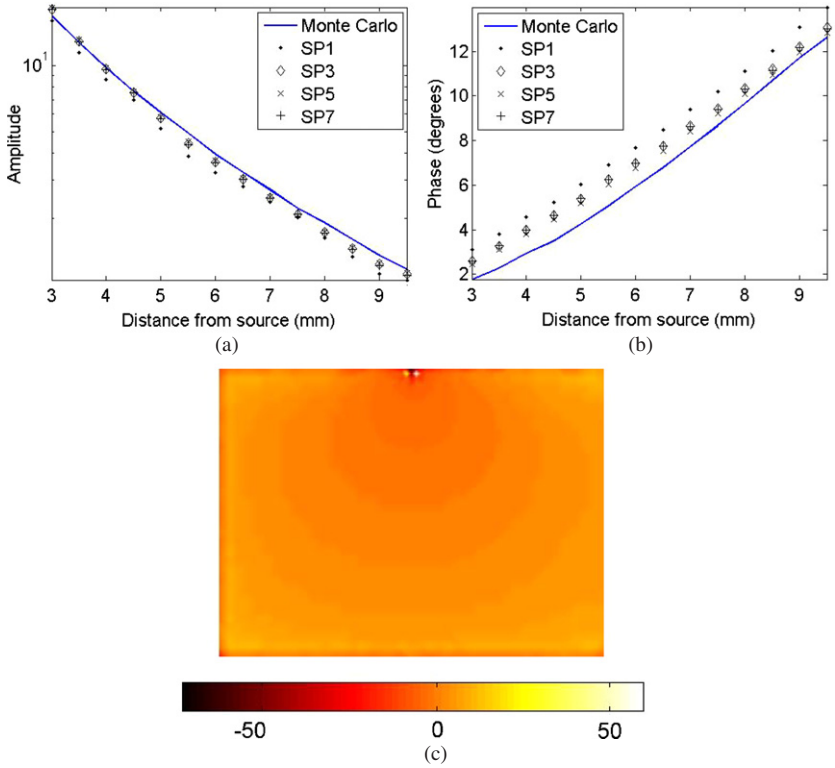

Figure 3. The calculated boundary data (a) log amplitude and (b) phase for SP_N and Monte Carlo model for uniform optical properties of $\mu_a = 0.001$ mm^{-1}, $\mu_s = 2.0$ mm^{-1}, $g = 0.5$ and $n_m = 1.37$; (c) is the cross-sectional percentage error between SP_7 and SP_1 for the calculated fluence at $y = 0$ mm corresponding to the plane at which the source is placed.

$y = 0$ mm shown in figure 3(c). As shown, the largest errors are seen near the source and detectors with errors as high as 60%.

Using a second homogenous model with optical properties of $\mu_a = 0.01$ mm^{-1}, $\mu_s = 2.0$ mm^{-1}, $g = 0.5$ and $n_m = 1.37$ the boundary measurements and internal fluence were also calculated and compared (figure 4). As in the previous case, SP_7 provides the best match for both amplitude and phase data, as compared to MC; however, the magnitude of the difference appears much greater due to the increased absorption. As shown in figure 4(c), errors of up to 60% are again seen between SP_1 and SP_7, specifically near the source.

In order to investigate the effects of a layered heterogeneous model of varied optical properties, the same 3D geometry as in previous cases was used, but containing three layers, as shown in figure 5. In this case, the model represents a three-layered case, whereby each layer has a thickness of 10 mm with the middle layer having a much stronger absorption (contrast of 200 in absorption) and scatter (contrast of 2 in scatter and increased anisotropic factor, g) as compared to the top and bottom layers. The results from both the SP_N and MC solution are shown in figure 6. The SP_5 and SP_7 models provide the best match with MC for both the amplitude and phase. The cross-section of the percentage error between SP_1 and SP_7, figure 6(c), again shows the largest error near the sources as well as the regions with and beyond the strong absorbing layer (layer 2). In this case, errors of up to 85% are seen

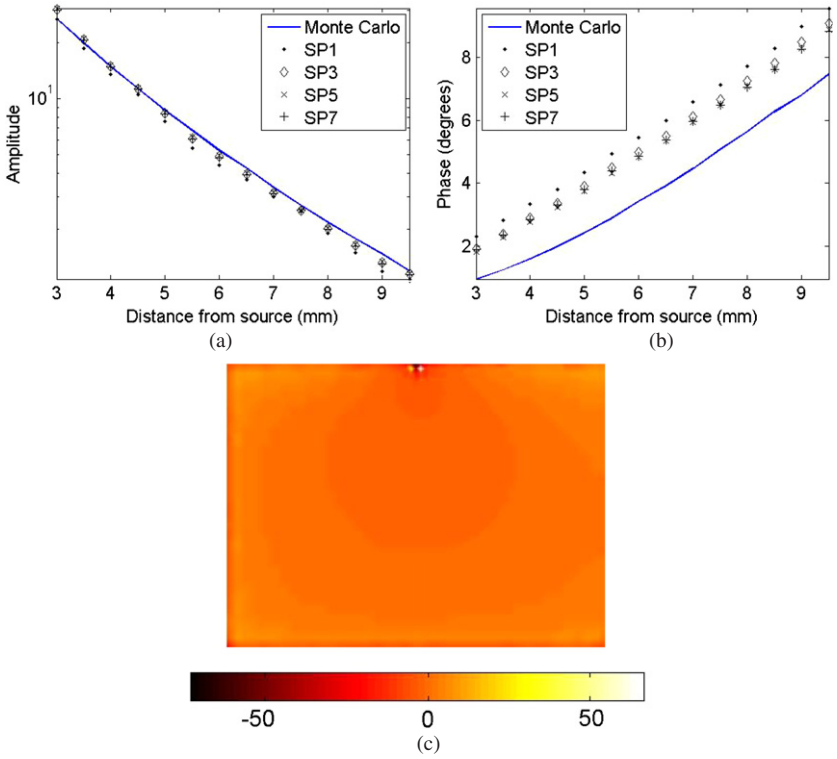

Figure 4. Same as figure 3, but for uniform optical properties of $\mu_a = 0.01\ \text{mm}^{-1}$, $\mu_s = 2.0\ \text{mm}^{-1}$, $g = 0.5$ and $n_m = 1.37$.

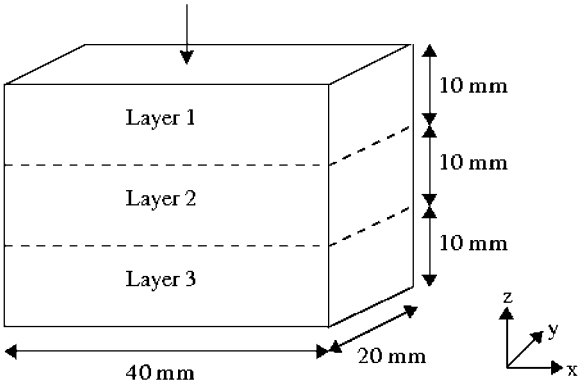

Figure 5. Schematic of the 3D layered model. Layers 1 and 3 have optical properties of $\mu_a = 0.001\ \text{mm}^{-1}$, $\mu_s = 1.0\ \text{mm}^{-1}$, $g = 0$ and $n_m = 1.37$ and layer 2 has optical properties of $\mu_a = 0.2\ \text{mm}^{-1}$, $\mu_s = 2.0\ \text{mm}^{-1}$, $g = 0.5$ and $n_m = 1.37$. The arrow indicates the location of the point source on the boundary.

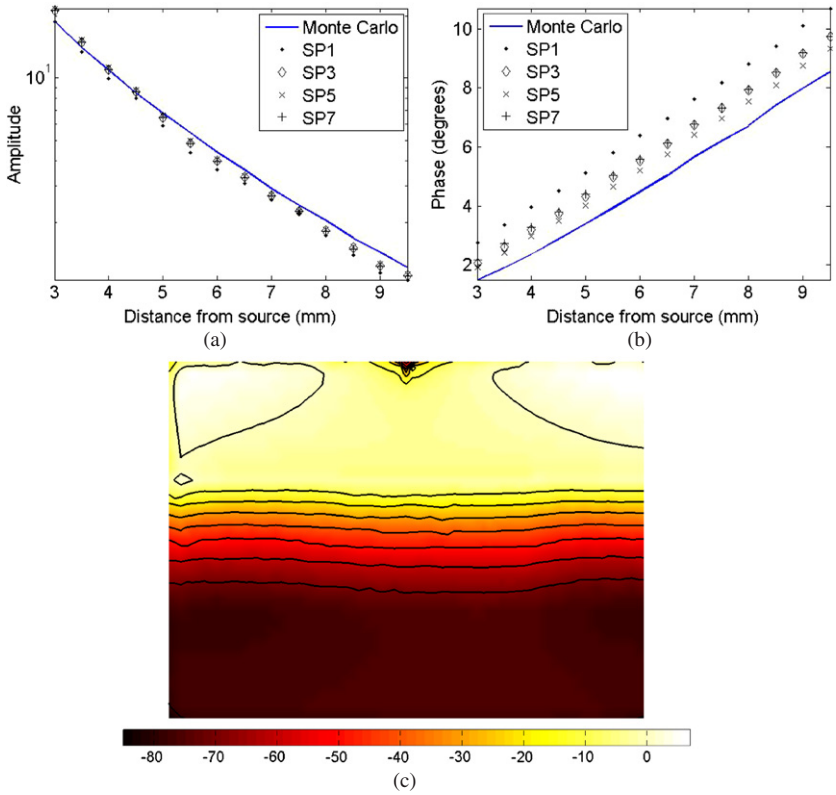

Figure 6. Same as figure 3, but for the layered model as shown in figure 5.

with layer 2, indicating that the solution of SP_1 to be dramatically different to that of SP_5 and SP_7.

4. Discussion

The calculated boundary data using MC and developed 3D frequency-domain modified simplified spherical harmonics expansion for three cases have been compared. In all the results presented, the data have not been scaled, nor any offset added, therefore providing the best means of comparison between different models and methods. In the first case, whereby the scattering properties were much higher than absorption ($\mu_a = 0.001\ \text{mm}^{-1}$, $\mu_s = 2.0\ \text{mm}^{-1}$, $g = 0.5$ and $n_m = 1.37$), figure 3, it is seen that the higher order SP_N models ($N > 1$) provide a much more accurate solution as compared with MC. Specifically, in the calculated amplitude data, it is seen that the solution using the SP_N models for $N = 3$, 5 and 7 provides the same degree of accuracy, whereas the diffusion approximation ($N = 1$) underestimates the magnitude of the calculated data. The errors seen in the phase, figure 3(b), are much greater with $N = 7$ providing the closest match as compared with MC. The magnitude of error seen with the calculated phase data reduces for measurements taken further away from the source, indicating that as the fluence becomes diffuse, the solutions converge, as expected in the diffusion approximation. In order to obtain a more quantitative analysis of the degree of error between $N = 1$ and $N = 7$, the percentage error between the total fluence calculated is shown

for a cross-section of the 3D model at $y = 0$ mm (directly under the source) (figure 3(c)). It is seen that the largest error (as large as 60%) is seen near the source, indicating that the suitability of the SP_N method lies within regions of close proximity to the source.

In the second case, whereby the absorbing properties were increased ($\mu_a = 0.01$ mm^{-1}, $\mu_s = 2.0$ mm^{-1}, $g = 0.5$ and $n_m = 1.37$), figure 4, the same trend of errors is seen as presented in the first case. However, the magnitude of differences between the phase data calculated using SP_N and MC is much higher, indicating the suitability of the SP_N method in higher absorption mediums. In this case again, the solution using $N = 1$ provides the least accurate solution as compared to MC. It was noticed that the phase data in figure 4 seemed to be poorer at greater distances from the source. This is most likely due to errors in the Monte Carlo model due to insufficient photons arriving at these detectors.

In order to evaluate the effect of layered models with much higher absorption, data using a layered MC and SP_N model are shown in figure 6. As with the previous cases, the calculated data using $N = 1$ provide the least accurate solution as compared to MC. Figure 6(c) shows the calculated error between the total fluence as obtained using $N = 1$ and $N = 7$. It is seen that the magnitude of error is largest not only near the source but also at the interface of two boundaries whereby the absorption coefficient increases. This is of importance given that some biological tissues, such as the liver which has a much higher blood content, will have a much greater absorption and appropriate modelling of such a situation is of paramount importance in small animal imaging. Similar results showing the effect of increased absorption within a medium have been shown in 2D (Klose and Larsen 2006).

It is interesting, and important to point out, that due to the asymptotic nature of the problem, no single order (N) will provide the most accurate solution. However, it is demonstrated here that the use of higher order approximations ($N > 1$) provides a much more accurate solution, specifically near source locations, which may be of importance when dealing with imaging of small volumes. Whilst it was seen that the SP_N data matched the MC data more closely than the diffusion data, they did not match perfectly. In order to make a like for like comparison, the data in all three cases have been shown without scaling or offsetting and as such, small differences between the two independent methods are unsurprising.

The amplitude and phase data in all three cases were studied only for the first 10 mm away from the source only. This has led to errors between the $SP_{N>1}$ and SP_1 data in cases even when scattering dominates over absorption since the light distribution is still forwardly biased near the source. As stated earlier, the validity of the diffusion approximation has been previously demonstrated for larger source/detector separation using both phantom data (Dehghani *et al* 2003a) and Monte Carlo data (Dehghani *et al* 2003a), and this work has concentrated in situation where the diffusion approximation is known to be inaccurate.

The timings for the SP_N and Monte Carlo models are displayed in table 1. It can be seen that the run-time of the Monte Carlo model was just seven times that of the SP_1 model and was in fact quicker than that of the SP_5 and SP_7 models which was unexpected. Due to the very large number of nodes in the FEM mesh, however, the Mass matrices were correspondingly large and their inversions required large amounts of memory. In the SP_5 and SP_7 cases, the memory requirements exceeded the physical memory available and therefore had to use 'swap space' which drastically increased the computation times. Also, the Monte Carlo data were obtained based on the paths of just 10^6 photons, a relatively small number of photons for Monte Carlo studies. A more quantitative study may use over ten times this number of photons leading to significantly longer computation times. In studies using meshes of lower resolutions where the use of swap space was not required, it was found that the SP_5 and SP_7 models took approximately $5t_d$ and $8t_d$ respectively where t_d is the computation time of the SP_1 model.

5. Conclusions

It is well known that the accuracy of the diffusion approximation is limited in regions of strong absorption and within regions before the NIR light becomes diffuse (i.e. near source locations). In such cases higher ordered approximations, such as the P_N and S_N methods, are required and whilst these methods have already been applied to tissue optics with promising results (Boas *et al* 1995, Aydin *et al* 2002), they both introduce a prohibitively large number of unknowns making them computationally expensive to solve. The SP_N approximation has the advantage of providing an increase in accuracy over the diffusion approximation whilst requiring fewer unknowns.

In this study, a three-dimensional frequency-domain light transport model based on the simplified spherical harmonics approximation has been developed. The model was used to calculate data for three individual cases with the results being compared to data obtained using a Monte Carlo model. In each of the three cases presented, the SP_N approximations with $N > 1$ were shown to provide an increase in accuracy over the SP_1 approximation in both the phase and amplitude of the boundary data. Comparisons of the fluence data from the SP_1 and SP_7 models showed that there is a significant difference in the regions surrounding the source where the light distribution is forwardly biased. The final case highlighted the limitations of the diffusion approximation in handling regions of strong absorption. Whilst the fluence data showed good agreement in the initial diffuse region, major differences of up to 85% were evident when the absorption was increased.

It was observed that the most accurate solution to a given problem was not necessarily provided by the highest ordered approximation, which has also been noted in previous studies into SP_N methods (Klose and Larsen 2006). This is due to the fact that unlike other methods which converge on the RTE solution as $N \rightarrow \infty$, the SP_N approximation only asymptotically approaches the RTE solution as N increases.

The effect of anisotropy has been previously demonstrated to be significant in highly absorbing media and must be modelled accurately using techniques presented here (Klose and Larsen 2006). The impact of modelling anisotropic scattering on image reconstruction is a subject of ongoing studies.

The SP_N methods would be of particular importance in imaging systems that utilize wavelengths approaching the visible region where absorption due to both oxygenized and deoxygenized haemoglobin is strong. As the SP_N methods require fewer equations, they are a more favourable forward model for image reconstruction.

The Monte Carlo model used in this study only calculated intensity data at a series of detectors located on the surface meaning that comparisons of internal fluence were not possible. Modifications to the Monte Carlo model to include the recording of internal fluence data are left for future work.

Acknowledgment

Funding for this work has been provided by the EPSRC. A D Klose has been supported in part by a grant (5U54CA126513-029001) from the National Institutes of Health (NIH).

Appendix

The individual system matrices of the FEM model, as represented by equations 10(*a*)–(*d*) can be represented by

$$K_{1_{ij}} = \int_{\Omega} \frac{1}{3\mu_{a1}}(r)\nabla u_i(r).\nabla u_j(r)\,\mathrm{d}^n r, \tag{A.1}$$

$$C_{_{ij}} = \int_{\Omega} \left(\mu_a(r) + \frac{\mathrm{i}\omega}{c(r)}\right) u_i(r)u_j(r)\,\mathrm{d}^n r, \tag{A.2}$$

$$C_{2_{ij}} = \int_{\Omega} \left(\frac{2}{3}\mu_a(r) + \frac{\mathrm{i}\omega}{c(r)}\right) u_i(r)u_j(r)\,\mathrm{d}^n r, \tag{A.3}$$

$$F_{1_{ij}} = \oint_{\partial\Omega} u_i(r)u_j(r)\,\mathrm{d}^{n-1} r, \tag{A.4}$$

and so on.

These system matrices can then be re-arranged for each composite moments of the fluence such that

$$M_{11} = K_1 + C + F_1, \tag{A.5}$$

$$M_{12} = -(C_1 + G_1), \tag{A.6}$$

$$M_{13} = C_2 + H_1, \tag{A.7}$$

$$M_{14} = -(C_3 + I_1), \tag{A.8}$$

$$M_{21} = K_3 + C_4 + C_5 + F_2, \tag{A.9}$$

$$M_{22} = -(C_1 + G_2), \tag{A.10}$$

$$M_{23} = -(C_6 + C_7 + H_2), \tag{A.11}$$

$$M_{24} = C_8 + C_9 + I_2, \tag{A.12}$$

$$M_{31} = K_5 + C_{10} + C_{11} + C_{12} + F_3, \tag{A.13}$$

$$M_{32} = C_2 + G_3, \tag{A.14}$$

$$M_{33} = -(C_6 + C_7 + H_3), \tag{A.15}$$

$$M_{34} = -(C_{13} + C_{14} + C_{15} + I_3), \tag{A.16}$$

$$M_{41} = K_7 + C_{16} + C_{17} + C_{18} + C_{19} + F_4, \tag{A.17}$$

$$M_{42} = -(C_3 + G_4), \tag{A.18}$$

$$M_{43} = C_8 + C_9 + H_4, \tag{A.19}$$

$$M_{44} = -(C_{13} + C_{14} + C_{15} + I_4). \tag{A.20}$$

References

Alexandrakis G, Rannou F R and Chatziioannou A F 2005 Tomographic bioluminescence imaging by use of a combined optical-PET (OPET) system: a computer simulation feasibility study *Phys. Med. Biol.* **50** 4225–41

Amestoy P R, Enseeiht-Irit, Davis T A and Duff I S 2004 Algorithm 837: AMD, an approximate minimum degree ordering algorithm *ACM Trans. Math. Softw.* **30** 381–8

Arridge S R 1999 Optical tomography in medical imaging *Inverse Problems* **15** R41–93

Arridge S R, Schweiger M, Hiraoka M and Delpy D T 1993 A finite element approach for modeling photon transport in tissue *Med. Phys.* **20** 299–309

Aydin E D, de Oliveira C R E and Goddard A J H 2002 A comparison between transport and diffusion calculations using a finite element-spherical harmonics radiation transport method *Med. Phys.* **29** 2013–23

Bluestone A Y, Abdoulaev G, Schmitz C, Barbour R L and Hielscher A H 2001 Three-dimensional optical-tomography of hemodynamics in the human head *Opt. Express* **9** 272–86

Boas D, Liu H, O'Leary M A, Chance B and Yodh A 1995 Photon migration within the P3 approximation *Proc. SPIE* **2389** 240–6

Case K M and Zweifel P F 1967 *Linear Transport Theory* (Reading, MA: Addison-Wesley)

Chandrasekhar S 1950 *Radiative Transfer* (London: Clarendon)

Choe R *et al* 2005 Diffuse optical tomography of breast cancer during neoadjuvant chemotherapy: a case study with comparison to MRI *Med. Phys.* **32** 1128–39

Contag C H and Bachmann M H 2002 Adavnces in *in vivo* bioluminescence imaging of gene expression *Annu. Rev. Biomed. Eng.* **4** 235–60

Corlu A, Choe R, Durduran T, Lee K, Schweiger M, Arridge S R, Hillman E M C and Yodh A G 2005 Diffuse optical tomography with spectral constraints and wavelength optimization *Appl. Opt.* **44** 2082–93

Dehghani H, Brooksby B, Vishwanath K, Pogue B W and Paulsen K D 2003a The effects of internal refractive index variation in near infrared optical tomography: a finite element modeling approach *Phys. Med. Biol.* **48** 2713–27

Dehghani H, Davis S C, Jiang S, Pogue B W, Paulsen K D and Patterson M S 2006 Spectrally-resolved bioluminescence optical tomography *Opt. Lett.* **31** 365–7

Dehghani H, Eames M E, Yalavarthy P K, Davis S C, Srinivasan S, Carpenter C M, Pogue B W and Paulsen K D 2008 Near infrared optical tomography using NIRFAST: algorithms for numerical model and image reconstruction algorithms *Commun. Numer. Methods Eng.* (doi:10.1002/cnm.1162)

Dehghani H, Pogue B W, Poplack S P and Paulsen K D 2003b Multiwavelength three-dimensional near-infrared tomography of the breast: initial simulation, phantom, and clinical results *Appl. Opt.* **42** 135–45

Enfield L C, Gibson A P, Everdell N L, Delpy D T, Schweiger M, Arridge S R, Richardson C, Keshtgar M, Douek M and Hebden J C 2007 Three-dimensional time-resolved optical mammography of the uncompressed breast *Appl. Opt.* **46** 3628–38

Gandjbakhche A H and Weiss G H 1995 *Random Walk and Diffusion-Like Models of Photon Migration in Turbid Media* (Amsterdam: North-Holland)

Gao F, Niu H, Zhao H and Zhang H 1998 The forward and inverse models in time-resolved optical tomography imaging and their finite-element method solutions *Image Vis. Comput.* **16** 703–12

Gelbard E M 1968 Spherical harmonic methods *Computing Methods in Reactor Physics* (New York: Gordon and Breach) chapter 4

Gibson A P, Hebden J C and Arridge S R 2005 Recent advances in diffuse optical imaging *Phys. Med. Biol.* **50** R1–43

Hebden J C, Gibson A, Austin T, Yusof R, Everdell N, Delpy D T, Arridge S R, Meek J H and Wyatt J S 2004 Imaging changes in blood volume and oxygenation in the newborn infant brain using three-dimensional optical tomography *Phys. Med. Biol.* **49** 1117–30

Hielscher A H, Alcouffe R E and Barbour R L 1998 Comparison of finite-difference transport and diffusion calculations for photon migration in homogeneous and heterogeneous tissues *Phys. Med. Biol.* **43** 1285–302

Hielscher A H, Klose A D and Hanson K M 1999 Gradient-based iterative image reconstruction scheme for time-resolved optical tomography *IEEE Trans. Med. Imaging* **18** 262–71

Jiang H and Paulsen K D 1995 A finite element based higher-order diffusion approximation of light propagation in tissues *Proc. SPIE* **2389** 608–14

Jiang H, Xu Y, Iftimia N, Eggert J, Klove K, Baron L and Fajardo L 2001 Three-dimensional optical tomographic imaging of breast in a human subject *IEEE Trans. Med. Imaging* **20** 1334–40

Jiang H B 1998 Frequency-domain fluorescent diffusion tomography: a finite-element-based algorithm and simulations *Appl. Opt.* **37** 5337–43

Klose A D and Beattie B J 2008 Bioluminescence tomography with SP3 equations *Biomedical Optics Topical Meeting Florida, The Optical Society of America (Washington, DC)*

Klose A D and Hielscher A H 1999 Iterative reconstruction scheme for optical tomography based on the equation of radiative transfer *Med. Phys.* **26** 1698–707

Klose A D and Hielscher A H 2003 Fluorescence tomography with simulated data based on the equation of radiative transfer *Opt. Lett.* **28** 1019–21

Klose A D and Larsen E W 2006 Light transport in biological tissue based on the simplified spherical harmonics equations *J. Comput. Phys.* **220** 441–70

Klose A D, Netz U, Beuthan J and Hielscher A H 2002 Optical tomography using the time-independent equation of radiative transfer: Part 1. Forward model *J. Quant. Spectrosc. Radiat. Transfer* **72** 691–713

Kuo C, Coquoz O, Troy T L, Xu H and Rice B W 2007 Three-dimensional reconstruction of *in vivo* bioluminescent sources based on multispectral imaging *J. Biomed. Opt.* **12** 24007

Larsen E W, Morel J E and McGhee J M 1996 Asymptotic derivation of the multigroup P-1 and simplified P-N equations with anisotropic scattering *Nucl. Sci. Eng.* **123** 328–42

Lathrop K D 1972 Discrete-ordinates methods for the numerical solution of the transport equation *React. Technol.* **15** 107–34

Mang T S, McGinnis C, Liebow C, Nseyo U O, Crean D H and Dougherty T J 1993 Fluorescence detection of tumors. Early diagnosis of microscopic lesions in preclinical studies *Cancer* **71** 269–76

Ntziachristos V 2006 Fluorescence molecular imaging *Annu. Rev. Biomed. Eng.* **8** 1–33

Ntziachristos V, Yodh A G, Schnall M and Chance B 2000 Concurrent MRI and diffuse optical tomography of breast after indocyanine green enhancement *Proc. Natl Acad. Sci. USA* **97** 2767–72

Reed W H 1971 New difference schemes for the neutron transport equation *Nucl. Sci. Eng.* **46** 309–14

Ren K, Abdoulaev G S, Bal G and Hielscher A H 2004 Algorithm for solving the equation of radiative transfer in the frequency domain *Opt. Lett.* **29** 578–80

Schweiger M, Arridge S R, Hiroaka M and Delpy D T 1995 The finite element model for the propagation of light in scattering media: boundary and source conditions *Med. Phys.* **22** 1779–92

Sevick-Muraca E M, Lopez G, Reynolds J S, Troy T L and Hutchinson C L 1997 Fluorescence and absorption contrast mechanisms for biomedical optical imaging using frequency-domain techniques *Photochem. Photobiol.* **66** 55–64

Srinivasan S, Pogue B W, Brooksby B, Jiang S, Dehghani H, Kogel C, Poplack S P and Paulsen K D 2005 Near-infrared characterization of breast tumors *in vivo* using spectrally-constrained reconstruction *Technol. Cancer Res. Treat.* **5** 513–26

Srinivasan S, Pogue B W, Carpenter C, Yalavarthy P K and Paulsen K D 2007 A boundary element approach for image-guided near-infrared absorption and scatter estimation *Med. Phys.* **34** 4545–57

Tarvainen T, Vauhkonen M, Kolehmainen V and Kaipio J P 2005 Hybrid radiative-transfer-diffusion model for optical tomography *Appl. Opt.* **44** 876–86

Vishwanath K, Pogue B W and Mycek M 2002 Quantitative fluorescence lifetime spectroscopy in turbid media: comparison of theoretical, experimental and computational methods *Phys. Med. Biol.* **47** 3387

Wang G, Cong W, Durairaj K, Qian X, Shen H, Sinn P, Hoffman H, McLennan G and Henry M 2006 *In vivo* mouse studies with bioluminescence tomography *Opt. Express* **14** 7801–9

Wang L, Jacques S L and Zheng L 1995 MCML—Monte Carlo modeling of photon transport in multi-layered tissues *Comput. Methods Programs Biomed.* **47** 131–46

Welch A J and Van Gemert M J C 1995 *Optical-Thermal Response of Laser Irradiated Tissue* (New York: Plenum)

Wright S, Schweiger M and Arridge S R 2007 Reconstruction in optical tomography using the P_N approximations *Meas. Sci. Technol.* **18** 79–86

Zacharopoulos A D, Arridge S R, Dorn O, Kolehmainen V and Sikora J 2006 Three-dimensional reconstruction of shape and piecewise constant region values for optical tomography using spherical harmonic parametrization and a boundary element method *Inverse Problems* **22** 1509–32

Zeff B W, White B R, Dehghani H, Schlaggar B L and Culver J P 2007 Retinotopic mapping of adult human visual cortex with high-density diffuse optical tomography *Proc. Natl Acad. Sci. USA* **104** 12169–74